A Miniature Fiber Collimator for Highly Sensitive Bend Measurements

Xizhen Xu, Jun He, *Member, OSA*, Maoxiang Hou, Shuhui Liu, Zhiyong Bai, Ying Wang, Changrui Liao, Zhengbiao Ouyang, and Yiping Wang, *Senior Member, OSA, Senior Member, IEEE*

Abstract—A Fabry–Perot interferometer (FPI) composed of a miniature fiber collimator is proposed and demonstrated for high-sensitivity bend measurements. The device consists of a quarter-pitch graded index fiber (GIF) spliced with a section of silica tube, which is interposed between single-mode fibers. The divergence angle of the included miniature fiber collimator was 0.058 rad, which was found to enhance the sensitivity of the proposed FPI to –3.353 dB/degree over the applied angle range. In comparison, the divergence angle without the collimator was 0.130 rad and FPI sensitivity was –0.618 dB/degree over the applied angle range. The fiber bend sensors demonstrated in this paper are compact, robust, and highly sensitive, and hence, are promising in various biomedical applications.

Index Terms—Fabry–Perot interferometers, optical fiber sensors, optical fiber devices.

I. INTRODUCTION

OPTICAL fiber sensors have been utilized in a variety of physical, chemical, and biological sensing studies. Their wide applicability is the result of many unique advantages, such as immunity to electromagnetic interference, compact size, high sensitivity, and durability in harsh environments. Among the physical parameters which have been quantified using optical fiber sensors, material bend has recently been attracting attention due to its significance in various engineering and structural monitoring applications.

Bend sensors have been fabricated using a wide range of techniques and materials. For example, Abdual *et al.* described a compound structure of single fiber Bragg grating (FBG) with an etched fiber segment [1]. However, the fabrication of this sensor required the use of 40% hydrofluoric acid (HF) as an etchant. In addition, the resulting sensitivity was relatively small (i.e., 0.43 dBm/degree). Frazão *et al.* used the combination of a long-period fiber grating (LPG) and a fused taper to measure the bend angle [2]. This sensor was only able to be used in transmission configuration and would not be preferable for single-ended sensor applications. Moreover, this sensor involved the complicated fabrication process of inscribing an LPFG. Liu *et al.* developed a bend senor using hollow core photonic crystal fibers with a relatively large measurement range (i.e., ±50°) [3]. However, hollow core photonic crystal fibers can be cost prohibitive. In addition, the wavelength interrogation was used in their work, and always requires complex and expensive wavelength demodulation devices. Recently, Bai *et al.* developed a bend senor based on a U-shaped Fabry-Perot cavity [4]. The device was fabricated by splicing a section of microfiber with two single mode fibers, a non-robust process.

In this study, we propose and demonstrate a novel bend sensor consisting of a Fabry-Perot interferometer (FPI). Optical fiber-based FPIs have been reported in a variety of studies for a wide range of applications. These devices exhibit several benefits, including easy fabrication, compact size, linear response, and high reliability. They have been utilized to measure physical parameters such as temperature [5], pressure [6], reflective index [7], [8], strain [9], and sound intensity [10]. Maintaining a high fringe visibility is critical with these devices as lower values result in a reduced signal-to-noise ratio (SNR). Fringe visibility was determined by the divergence angle of the beam split from the first reflected FPI surface [11]. A collimator could be used to reduce this divergence angle and fabricate an FPI with sufficiently high fringe visibility. In previous studies, graded refractive index (GRIN) lenses were used as optical collimators. However, GRIN-lens-based collimators are always quite bulky. Graded index fibers (GIF) have also been used to create optical collimators in many applications such as probes in optical coherence tomography [12], low-loss optical connectors [13], and optofluidic tunable manipulation [14]. A high fringe visibility FPI can be fabricated from quarter-pitch graded index fibers, which function as a collimator-like micro GRIN lens [15], [16].

The FPI proposed in this study was fabricated by splicing a section of silica tube with a quarter-pitch GIF-based collimator and a single mode fiber (SMF). The air cavity between the GIF end face and the SMF serves as an FPI cavity and a direct sensing head. The divergence angle of the beam exiting from the

X. Xu, J. He, M. Hou, S. Liu, Z. Bai, Y. Wang, C. Liao, and Y. Wang are with the Key Laboratory of Optoelectronic Devices and Systems of Ministry of Education and Guangdong Province, College of Optoelectronic Engineering, Shenzhen University, Shenzhen 518060, China (e-mail: 406434774@qq.com; hejun07@szu.edu.cn; maoxiangh@szu.edu.cn; liushuhui@szu.edu.cn; baizhiyong@szu.edu.cn; yingwang@szu.edu.cn; cliao@szu.edu.cn; ypwang@szu.edu.cn).

Z. Ouyang is with the College of Electronic Science and Technology, Shenzhen University, Shenzhen 518060, China (e-mail: zbouyang@126.com).

Color versions of one or more of the figures in this paper are available online at http://ieeexplore.ieee.org.
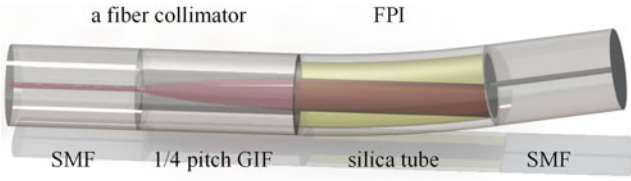
Fig. 1.   A schematic diagram of a GIF-FPI in the bending state.

quarter-pitch GIF was measured experimentally and found to be smaller than the SMF. The fringe visibility enhancement of the GIF-FPI was experimentally validated and compared with that of a conventional SMF-FPI. Theoretical results suggested that the GIF-FPI can be used to detect bend angles. Fringe visibility was found to decrease when the GIF-FPI was applied with a given bend angle.

II. DEVICE STRUCTURE AND WORKING PRINCIPLES

Fig. 1 shows an illustration of the proposed GIF-FPI, fabricated by splicing a section of silica tube with a fiber collimator and single mode fiber (SMF). The fiber collimator was fabricated by splicing an SMF and a quarter-pitch GIF. Gaussian beam approximation was used to establish a theoretical model for the fiber collimator [17]. In this approach, an output beam from a fiber collimator is assumed to have the cross-sectional intensity distribution of a Gaussian profile. The radial output beam waist (ω_{GIF}) from the fiber collimator can be calculated with the following ray matrix model [18]:

$$\omega_{\mathrm{GIF}} = \frac{\omega_0}{(\pi\omega_0^2/\lambda)\cdot n\cdot g} \cdot \left[\sin^2\left(g\cdot L_{\mathrm{GIF}}\right)\right.$$
$$\left. + (\lambda/\pi\omega_0^2 ng)^2 \cdot \cos^2\left(g\cdot L_{\mathrm{GIF}}\right)\right]^{-1/2}, \quad (1)$$

where ω_0 is the radial beam waist of the mode field for a single mode fiber, n is the center refractive index of the GIF core, L_{GIF} is the GIF length, g is the GIF focusing parameter defined as $g = \sqrt{2\Delta}/a$, and Δ and a are the fractional index changes at the core-cladding interface and the GIF core radius, respectively.

The divergence angle of the output beam can be approximated as:

$$\theta_0 = \frac{\lambda}{\pi\omega_{\mathrm{GIF}}}. \quad (2)$$

A quarter-pitch GIF was introduced to construct an FPI with enhanced fringe visibility. Due to low reflectivity at the fiber/air interface, multiple reflections were neglected. This low finesse FPI can be modeled using a two-beam optical interference equation:

$$I = I_1 + I_2 + 2\sqrt{I_1 I_2}\cos\varphi, \quad (3)$$

where I is the intensity of the interference signal, I_1 and I_2 are the reflection at the two cavity surfaces, and φ is the optical phase difference between the two rays reflected at the two cavity surfaces.

Fig. 2(a) demonstrates the ray splitting from the GIF end and transferring into the FPI cavity. The ray is then reflected by surface II, transferred again into the cavity, and interferes with the ray reflected by surface I. The term I_{m1} is the intensity of
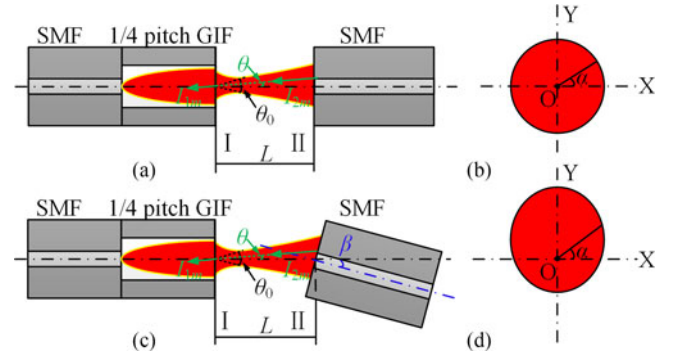

Fig. 2.   (a) A schematic of the proposed collimator-based FPI; (b) the beam profile on surface II; (c) a schematic of the FPI with an induced bend angle; (d) the beam profile on surface II with an induced bend angle.

the ray reflected by surface I and I_{m2} is the intensity of the ray reflected by surface II. The term I_m is the intensity resulting from the interference of I_{m1} and I_{m2}. It can be expressed as [19]:

$$I_m = \frac{I_0}{\Delta\varphi}\left[R + (1-R)^2 R + 2R(1-R)\cos\varphi\right]. \quad (4)$$

Calculating the total intensity I resulting from the interference of I_1 and I_2 requires the integration of (5):

$$I = \int_{\varphi_0 - \Delta\varphi_{\max}}^{\varphi_0} I_m(\varphi)\, d\varphi. \quad (5)$$

where I_0 is the total intensity of the ray incident on the cavity, R is the Fresnel reflection coefficient of surfaces I and II, φ_0 is the maximum of the optical phase difference φ, $\Delta\varphi$ is the optical phase dispersion (i.e., the deviation of φ from φ_0), and $\Delta\varphi_{\max}$ is the maximum of $\Delta\varphi$.

From this expression, the fringe visibility is determined to be:

$$V = \frac{I_{\max} - I_{\min}}{I_{\max} + I_{\min}}. \quad (6)$$

According to (4)-(6), the total interference intensity I and the fringe visibility V can be calculated as follows:

$$I = I_0\left(R + (1-R)^2 R\right) + I_0\left(2(1-R)R\cdot\frac{\sin\left(\Delta\varphi_{\max}/2\right)}{\Delta\varphi_{\max}/2}\right.$$
$$\left.\times\cos\left(\varphi_0 - \frac{\Delta\varphi_{\max}}{2}\right)\right), \quad (7)$$

$$V = \frac{2R(1-R)}{R + (1-R)^2 R}\cdot\frac{\sin\left(\Delta\varphi_{\max}/2\right)}{\Delta\varphi_{\max}/2}. \quad (8)$$

The FPI has a maximum fringe visibility of 1, when light reflected from the two cavity surfaces is of equal intensity ($I_1 = I_2$). However, optical losses increase when the two cavity end faces are not parallel or absorption occurs in the medium filling the cavity. The dominant effect is caused by a recoupling loss in the air cavity with two parallel surfaces, as divergence of light from the lead-in fiber end surface is inevitable. Optical losses also increase as the cavity length increases. The divergence angle of a quarter-pitch GIF is smaller than that of a single mode fiber,

which can function as a collimator. The fringe visibility of an FPI based on a quarter-pitch GIF can be increased.

The beam profile on surface II is circular when a bend angle has not yet been introduced, as shown in Fig. 2(b). The optical phase difference of the rays reflected by surfaces I and II is given by [20]:

$$\varphi\left(\theta\right) = \varphi_0 \cos\theta = \frac{4\pi n L}{\lambda} \cos\theta, \quad \left(0 \leq \theta < \theta_0/2\right) \quad (9)$$

where n is the refractive index of the medium filling the FPI cavity, L is the length of the FPI cavity, λ is the optical wavelength in a vacuum, θ_0 is the divergence angle of the quarter-pitch GIF, and θ is the internal angle of the ray ranging from 0 to $\theta_0/2$. These values are independent of the angle α between the OX and OY axes. The angle θ assumes a maximum value of $\theta_0/2$ in short FPI cavities. The term φ_0 is the optical phase of light along the fiber axis and is given by $4\pi n L/\lambda$.

The term $\Delta\varphi(\theta)$ is the optical phase dispersion and is a measure of the range of optical path lengths taken by interfering beams at various integral angles θ within the interferometer. It can be expressed as [20]:

$$\Delta\varphi\left(\theta\right) = \varphi_0 \left(1 - \cos\theta\right). \quad \left(0 \leq \theta < \theta_0/2\right) \quad (10)$$

The resulting interference intensity and fringe visibility have been evaluated with the induced bend angle shown in Fig. 2(c). The intensity I_1 is unaffected by the introduction of this bend angle but I_2 decreases. This is because the beam splits from the GIF end face and propagates through a cavity length distance of L. The intensity I_2 is determined by the divergence angle θ_0 as smaller divergence angles allow more light to be reflected back into the FPI cavity and recoupled with the lead-fiber. Relatively small divergence angles can be obtained using a quarter-pitch GIF. However, the beam profile on surface II deforms into an ellipse when the bend angle shown in Fig. 2(d) is introduced.

Only a fraction of the light can be guided back to surface I after being reflected by surface II. The maximum internal ray angle which can be reflected by surface II and guided back to surface I is given by [20]:

$$\theta_b\left(\alpha\right) = \beta\cos\alpha + \frac{\theta_0}{2}\left[1 - \left(\frac{2\beta\sin\alpha}{\theta_0}\right)^2\right], \quad (11)$$

where β is the bend angle and α is the angle between the OX and OY axes.

The term $\Delta\varphi^b(\theta)$ is $\Delta\varphi(\theta)$ with an induced bend angle, and can be expressed as:

$$\Delta\varphi^b\left(\theta\right) = \varphi_0\left(1 - \cos\theta\right). \quad \left(0 \leq \theta \leq \theta_b\right) \quad (12)$$

According to (11) and (12), $\Delta\varphi^b_{\max}$ is the maximum of $\Delta\varphi^b$, which can be calculated as follows:

$$\Delta\varphi^b_{\max} = \varphi_0\left(1 - \cos\theta_b\right). \quad (13)$$

Substitute (11) and (13) into (4) and (5). The intensity resulting from interference at surfaces I and II can be obtained by integrating over a range of angles α between 0 and 2π,

as follows:

$$I = I_0\left(R + \left(1 - R\right)^2 R\right) + I_0 \cdot 2\left(1 - R\right)R$$

$$\cdot \frac{1}{2\pi}\int_0^{2\pi}\frac{1}{\Delta\varphi^b_{\max}\left(\alpha,\beta\right)}\int_{\varphi_0 - \Delta\varphi^b_{\max}}^{\varphi_0}\cos\varphi\left(\alpha,\beta\right)d\varphi d\alpha$$

$$= I_0\left(R + \left(1 - R\right)^2\right) + I_0 \cdot 2\left(1 - R\right)R$$

$$\cdot \frac{1}{2\pi}\int_0^{2\pi}\frac{\sin\left[\Delta\varphi^b_{\max}\left(\alpha,\beta\right)/2\right]}{\Delta\varphi^b_{\max}\left(\alpha,\beta\right)/2}$$

$$\cos\left[\varphi_0 - \frac{\Delta\varphi^b_{\max}\left(\alpha,\beta\right)}{2}\right]d\alpha. \quad (14)$$

A numerical solution to the (14) can then be obtained. Fringe visibility can be evaluated by (6), which decreases as bend angles increases.

III. FABRICATION AND CHARACTERIZATION OF A MINIATURE FIBER COLLIMATOR

A GIF collimator was fabricated by splicing a quarter-pitch GIF (Yangtze Optical Fiber, 62.5/125GI 0.275) to a single mode fiber (Corning G652D). A GIF with an exact length can then be cut using a fiber-processing system with an error of ± 10 μm. This device was fabricated with two precision translation stages (Thorlabs XR25P/M), a fiber cleaver (Sumitomo FC-6S), and a microscope (Sunway). To validate the expression in (2), it was necessary to measure the divergence angle as a function of GIF length. This was done using the experimental setup shown in Fig. 3(a). Light from a tunable laser (Agilent 81940A, central wavelength: 1550.00 nm) was incident on an SMF spliced with a GIF collimator held fixed by a fiber holder. The output end face of the GIF collimator was positioned parallel to the receiving surface of an infrared CCD (Newport LBP2-HR-IR2) by adjusting the stage under the GIF collimator. The intensity profile was collected by the beam profiler and stored to a computer. A variable optical attenuator (VOA) was used to avoid saturation of infrared CCD pixels. Fig. 3(c) shows the divergence angle measurement configuration. Fig. 3(b) shows a sample output beam optical profile from the GIF collimator, obtained using the infrared CCD. The $1/e^2$ beam diameter and maximum intensity could then be calculated.

We measured the divergence angles of GIFs with different lengths. It is obvious from Fig. 4(a) that the beam diameter increased linearly as the distance between the CCD and GIF increased in the far field. The divergence angle of the output beam was calculated from the following equation:

$$\theta_0 = 2 \cdot \frac{\omega_{d2} - \omega_{d1}}{d_2 - d_1}, \quad (15)$$

where ω_{d2} and ω_{d1} are the beam radius at distances of d_2 and d_1, respectively. The divergence angle θ_0 can be calculated from the slope of the beam diameter as a function of distance, as shown in Fig. 4(a).

The GIF divergence angles at GIF lengths ranged from 0–520 μm were measured and shown in Fig. 4(b). It could be clearly seen that the divergence angle varies as a cosine
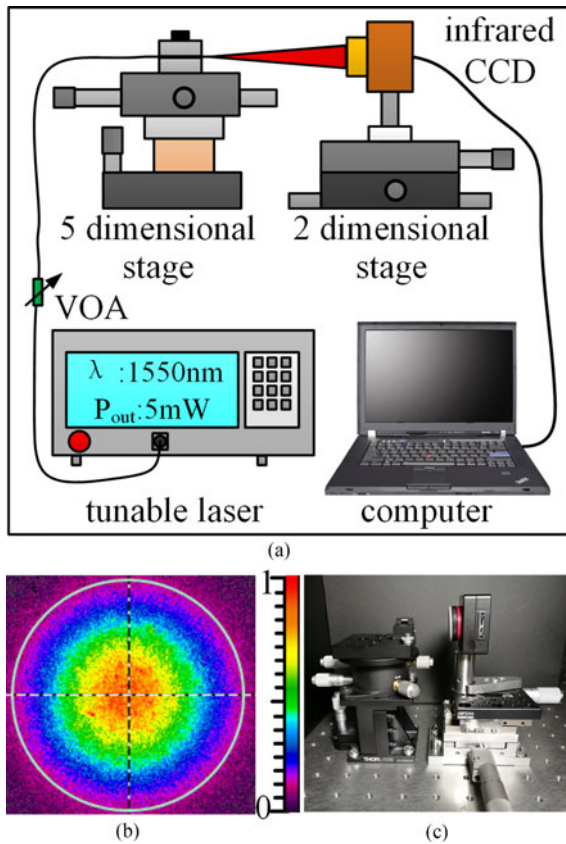
Fig. 3. (a) A schematic diagram of the divergence angle measurement configuration; (b) a far-field IR image obtained with an infrared CCD; (c) an image of the divergence angle measurement setup.
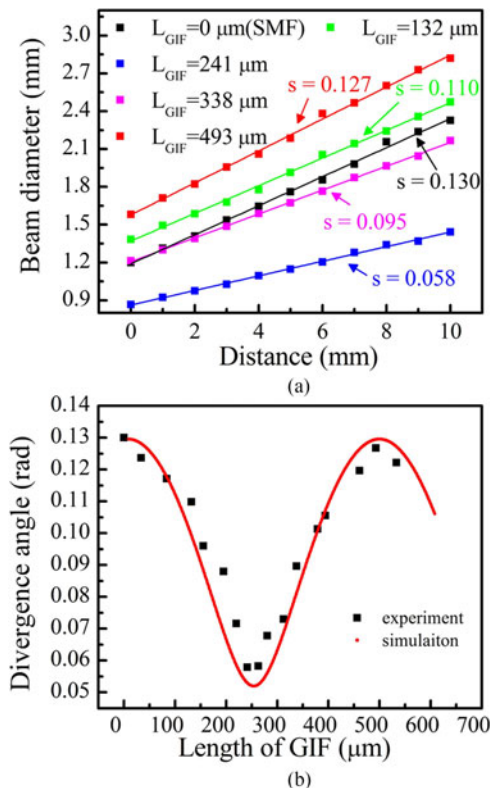

Fig. 4. (a) Beam diameter response as a function of distance; (b) divergence angles as a function of GIF length.
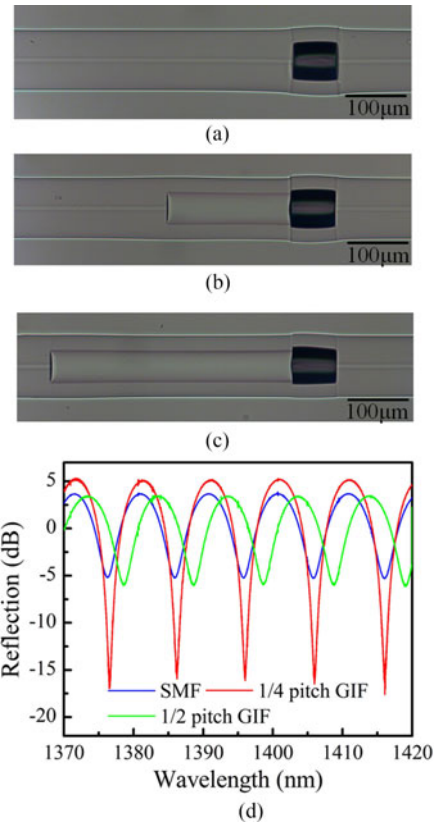

Fig. 5. (a)–(c) Microscope images of the SMF-FP, 1/4 pitch GIF-FP, and 1/2 pitch GIF-FP at the same cavity length of 98 μm, respectively; (d) reflection spectra for the SMF-FP, 1/4 pitch GIF-FP, and 1/2 pitch GIF-FP at the same cavity length of 98 μm.

function of the GIF length. For example, the minimum divergence angle was 0.058 rad and achieved at a GIF length of 245 μm. In contrast, the maximum two divergence angles (i.e., 0.130 and 0.127 rad) were achieved at the output of an SMF without GIF and a GIF with a length of 490 μm, respectively. Moreover, the simulation results, as shown in the red curve in Fig. 4(b), agree well with the measurement results. These results demonstrate that the GIF has a focusing period, i.e., the quarter pitch of GIF is about 245 μm and the half pitch of GIF is about 490 μm. As a result, a collimator has been successfully fabricated by splicing an SMF with a GIF of appropriate length (i.e., a quarter pitch).

IV. FABRICATION OF FABRY-PEROT INTERFEROMETERS WITH INCREASED FRINGE VISIBILITY

A GIF collimator was investigated to enhance fringe visibility in FPI cavities of various lengths. A GIF-FPI was fabricated by splicing a GIF collimator with a section of silica tube and a well-cut SMF. The FPI reflection spectra were investigated using a 1×2, 3 dB fiber coupler connecting a super-luminescent source and an optical spectrum analyzer (OSA). Fig. 5(a)–(c) shows microscope images for an SMF-FPI, a quarter-pitch (245 μm) GIF-FPI, and a half-pitch (490 μm) GIF-FPI, respectively, and the corresponding reflection spectra were demonstrated in Fig. 5(d). Each of these devices had approximately the same
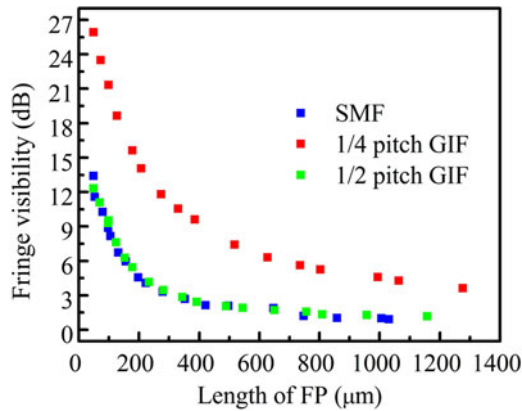
Fig. 6. A fringe visibility comparison between the SMF-FPI, a quarter-pitch GIF-FPI (245 μm), and a half-pitch (490 μm) GIF-FPI.

Fig. 7. (a) A microscope image of a quarter-pitch (245 μm) GIF-FPI with a cavity length of 300 μm; (b) a microscope image of an SMF-FPI with a cavity length of 300 μm; (c) the experimental setup for bend angle measurements.

cavity length ($\sim$98 μm). Fringe visibility for the SMF-FPI and half-pitch (490 μm) GIF were $\sim$9 dB, while that of the quarter-pitch (245 μm) GIF-FPI was 23 dB. These results indicate that the fringe visibility can be enhanced by decreasing the divergence angle.

In order to evaluate the fringe visibility of various cavity lengths, we investigated an SMF-FPI, a quarter-pitch (245 μm) GIF-FPI, and a half-pitch (490 μm) GIF-FPI. Each SMF, the quarter-pitch (245 μm) GIF, and the half-pitch (490 μm) GIF with a well-cut end face had been fabricated. An additional single mode fiber with a well-cut face was used as the second reflected FPI surface. A quarter-pitch (245 μm) GIF with a well-cut face and an SMF with a well-cut face were fixed on a commercial fusion splicer (Fujikura-60S). Various FPI cavity lengths were obtained using a high precision motor in the commercial fusion splicer. The FPI reflection spectra for varying cavity lengths were analyzed using a 1$\times$2, 3 dB fiber coupler connecting a super-luminescent source and an optical spectrum analyzer (OSA). The fringe visibility of SMF-FPIs with various cavity lengths and a half-pitch (490 μm) GIF-FPI were evaluated using the above method. Fig. 6 shows a plot of fringe visibility as a function of FP cavity length for an SMF-FPI, a quarter-pitch (245 μm) GIF-FPI, and a half-pitch (490 μm) GIF-FPI. In each case, visibility decreased with increasing cavity length. However, it is evident the fringe visibility of the quarter-pitch (245 μm) GIF-FPI was higher than that of the other two, with an FPI cavity length ranging from 50-1300 μm. These results demonstrate that an FPI with high fringe visibility can be fabricated with different cavity lengths using a quarter-pitch (245 μm) GIF.

V. BEND RESPONSE OF FABRY-PEROT INTERFEROMETRIC SENSORS

FPI fringe visibility can be strongly affected by the degree of parallelism between the two reflected surfaces. Hence, a quarter-pitch (245 μm) GIF-FPI can be used as a highly sensitive bend angle sensor by measuring the resulting fringe visibility.

A quarter-pitch (245 μm) GIF-FPI with a cavity length of 300 μm was used to test sensitivity to bend angle and an SMF-FPI was included for comparison. Fig. 7(a) and (b) shows
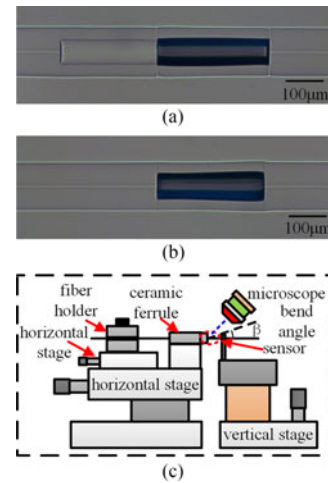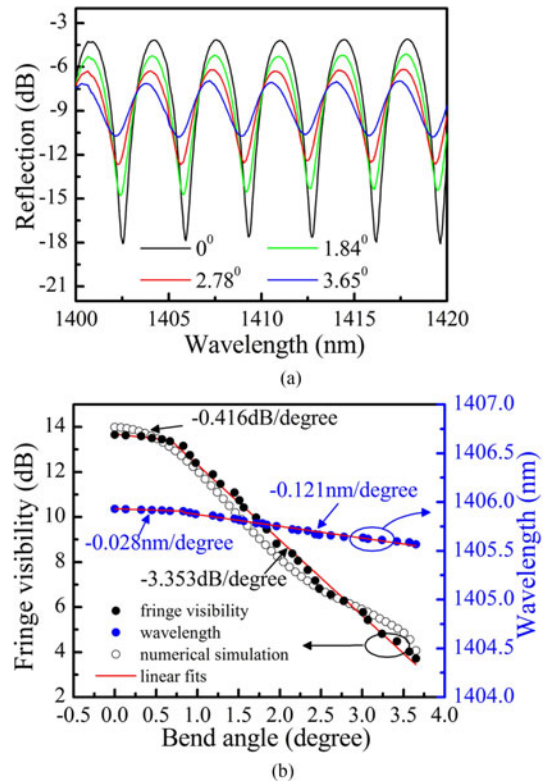

Fig. 8. (a) Reflection spectra for a quarter-pitch (245 μm) GIF-FPI with a cavity length of 300 μm at bend angles of 0°, 1.84°, 2.78°, and 3.65°; (b) bend angle response for a quarter-pitch (245 μm) GIF-FPI with a cavity length of 300 μm.

microscope images of a quarter-pitch GIF-FPI (245 μm) with a cavity length of 300 μm and an SMF-FPI with a cavity length of 300 μm, respectively. Fig. 7(c) shows a schematic of the bend angle measurement apparatus. The fiber holder was installed on the upper horizontal stage. These and the ceramic ferrule with a 130 μm inner diameter were mounted on the outer horizontal stage. The sample was then fixed on the fiber holder and moved
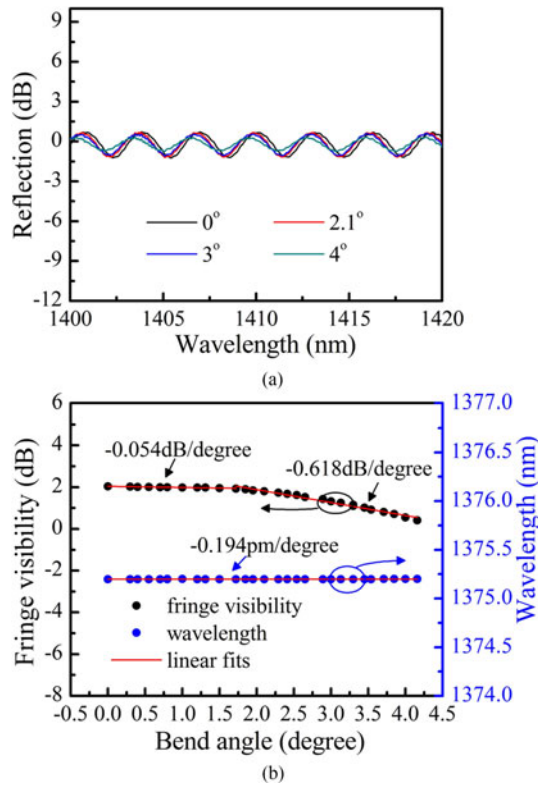
Fig. 9.　(a) reflection spectra for an SMF-FPI with a cavity length of 300 μm at bend angles of 0°, 2.1°, 3°, and 4°; (b) bend angle response for the SMF-FPI with a cavity length of 300 μm.

into the ceramic ferrule horizontally. Motion ceased when the FPI cavity section used as a sensor emerged from the front end of the ceramic ferrule. Various bend angles could be achieved by raising the mandrel, which were then observed and calculated using a microscope. Reflection spectra were assessed using a 1 × 2, 3dB fiber coupler connecting a super- luminescent source and an optical spectrum analyzer (OSA).

As shown in Fig. 8(a), the reflection spectra for the quarter-pitch (245 μm) GIF-FPI exhibited a strong dependence on bend angles ranging from 0° to 3.65°. This spectral variation is shown in Fig. 8(b), in which the piecewise linear fitting was adopted to obtain the bend sensitivity of the device. It is evident that the sensitivity of −0.416 dB/degree is lower for angles ranging from 0° to 0.7°. As the angle increased, this sensitivity was enhanced to −3.353 dB/degree for angles ranging from 0.7° to 3.65°. Moreover, the wavelength response was −0.028 nm/degree for angles ranging from 0° to 0.7° and −0.121 nm/degree for angles ranging from 0.7° to 3.65°. We calculated the fringe visibility of GIF-FPI as a function of bend angle based on (12)–(14) via MATLAB. It is evident from Fig. 8(b) the experimental results agree well with the numerical simulation results.

In comparison, Fig. 9(a) indicates the SMF-FPI had a much weaker variation ranging from 0° to 4.0°. As shown in Fig. 9(b), the bend sensitivity of the SMF-FPI ranges from 0° to 0.7° and 1.5° to 4.0° were −0.054 dB/degree and −0.618 dB/degree, respectively. The wavelength response of −0.194 pm/degree was negligible for angles ranging from 0° to 4.0°. These results

indicate that the bend sensitivity of this device could be increased drastically with the aid of a quarter-pitch GIF.

In addition, it should be noted that the maximum bend angle measured in the experiments was limited by the mechanical strength of the silica tube and fusion splicing joints. The small bend measurement range demonstrated in this work might be sufficient for some specific applications such as large-span structural health monitoring, in which the bend measurement accuracy is more important. Moreover, the bend measurement range of this device could further be increased using a longer silica tube. In this case, the GIF-based miniature collimator will also be helpful to improve the fringe visibility of a long-cavity FPI, as shown in Fig. 6.

VI. CONCLUSION

We proposed and demonstrated a low-cost fiber optic device based on a miniature fiber collimator Fabry-Perot interferometer (FPI) for bend angle measurements. The device is compact and easy to fabricate. The miniature fiber collimator was formed by a single mode fiber spliced with a quarter-pitch (245 μm) GIF. It exhibited a divergence angle of 0.058 rad, which is significantly less than the 0.130 rad achieved with a single mode fiber. FPI fringe visibility was vastly enhanced using a miniature fiber collimator, achieving a bend angle sensitivity of −3.353 dB/degree ranging from 0.7° to 3.65°. This value is much higher than the −0.618 dB/degree obtained without a miniature collimator. The fiber bend sensors proposed in this paper could further be developed as high-performance measurement probes in various biomedical applications.

REFERENCES

[1] A. Rauf, J. Zhao, and B. Jiang, "Bend measurement using an etched fiber incorporating a fiber Bragg grating," *Opt. Lett.*, vol. 38, no. 2, pp. 214–216, 2013.

[2] O. Frazão, R. Falate, and J. L. Fabris, "Optical inclinometer based on a single long-period fiber grating combined with a fused taper," *Opt. Lett.*, vol. 31, no. 20, pp. 2960–2962, 2006.

[3] S. Liu, N. Liu, and M. Hou, "Direction-independent fiber inclinometer based on simplified hollow core photonic crystal fiber," *Opt. Lett.*, vol. 38, no. 4, pp. 449–451, 2013.

[4] Z. Bai *et al.*, "Torsion sensor with rotation direction discrimination based on a pre-twisted in-fiber Mach–Zehnder interferometer," *IEEE Photon. J.*, vol. 9, no. 3, Jun. 2017, Art. no. 7103708.

[5] T. Wei, Y. Han, H. Tsai, and H. Xiao, "Miniaturized fiber inline Fabry-Perot interferometer fabricated with a femtosecond laser," *Opt. Lett.*, vol. 33, no. 6, pp. 536–538, 2008.

[6] C. R. Liao, S. Liu, L. Xu, and C. Wang, "Sub-micron silica diaphragm-based fiber-tip Fabry-Perot interferometer for pressure measurement," *Opt. Lett.*, vol. 39, no. 10, pp. 2827–2830, 2014.

[7] T. Wei, Y. Han, Y. Li, and H. Xiao, "Temperature-insensitive miniaturized fiber inline Fabry-Perot interferometer for highly sensitive refractive index measurement," *Opt. Express*, vol. 16, no. 8, pp. 5764–5769, 2008.

[8] X. Xu *et al.*, "Growth dynamics of ZnO nanowire on a fiber-tip air bubble," *Opt. Mater. Express*, vol. 7, no. 9, pp. 3433–3440, 2017.

[9] S. Liu, K. Yang and Y. Wang, "High-sensitivity strain sensor based on in-fiber rectangular air bubble," *Sci. Rep.*, vol. 5, pp. 7624, 2015.

[10] P. C. Beard and T. N. Mills, "Extrinsic optical-fiber ultrasound sensor using a thin polymer film as a low-finesse Fabry-Perot interferometer," *Appl. Opt.*, vol. 35, no. 4, pp. 663–675, 1996.

[11] M. Han and A. Wang, "Exact analysis of low-finesse multimode fiber extrinsic Fabry-Perot interferometers," *Appl. Opt.*, vol. 43, no. 24, pp. 4659–4666, 2004.

[12] Y. Qiu, Y. Wang, and K. D. Belfield, "Ultrathin lensed fiber-optic probe for optical coherence tomography," *Biomed. Opt. Express*, vol. 7, no. 6, pp. 2154–2162, 2016.

[13] D. Ouyang, S. Ruan, C. Guo, and H. Wei, "Low loss splicing between double-clad fiber and photonic crystal fiber using graded index fiber lens," *J. Lightw. Technol.*, vol. 32, no. 14, pp. 2524–2530, Jul. 2014.

[14] Y. Gong, C. Zhang, and Q. F. Liu, "Optofluidic tunable manipulation of microparticles by integrating graded-index fiber taper with a microcavity," *Opt. Express*, vol. 23, no. 3, pp. 3762–3769, 2015.

[15] C. A. Jack and W. L. Emkey, "Analysis and evaluation of graded-index fiber lenses," *J. Lightw. Technol.*, vol. 5, no. 9, pp. 1156–1164, Sep. 1987.

[16] D. V. Baranov, I. V. Zhurilova, and S. K. Isaev, "Fiber-optic Fabry-Perot interferometers utilizing graded-index optical waveguides," *Sov. J. Quantum Electron.*, vol. 19, no. 5, pp. 690–692, 1989.

[17] V. Arya, M. D. Vries, and K. A. Murphy, "Exact analysis of the extrinsic Fabry-Perot interferometric optical fiber sensor using Kirchhoff's diffraction formalism," *Opt. Fiber Technol.*, vol. 1, no. 4, pp. 380–384, 1995.

[18] Y. Zhang *et al.*, "Fringe visibility enhanced extrinsic Fabry-Perot interferometer using a graded index fiber collimator," *IEEE Photon. J.*, vol. 2, no. 3, pp. 469–481, Jun. 2010.

[19] J. L. Santos, A. P. Leite, and D. A. Jackson, "Optical fiber sensing with a low-finesse Fabry-Perot cavity," *Appl. Opt.*, vol. 31, no. 34, pp. 7361–7366, 1992.

[20] F. Pérennès, P. C. Beard, and T. N. Mills, "Analysis of a low-finesse Fabry-Perot sensing interferometer illuminated by a multimode optical fiber," *Appl. Opt.*, vol. 38, no. 34, pp. 7026–7034, 1999.

Shuhui Liu was born in Hubei, China, in 1989. In 2015, he joined the School of Physics, Wuhan Institute of Technology, as a Lecturer. His research interests are optical fiber sensing and femtosecond laser micromachining.

Zhiyong Bai was born in Henan, China, in 1984. He is currently with Shenzhen University, Shenzhen, China, as an Assistant Professor. His current research interests include optical fiber gratings, orbital angular momentum, and optical fiber sensors.

Ying Wang was born in Henan, China, in 1983. He is currently with Shenzhen University, Shenzhen, China, as an Associate Professor. His research interests are optical fiber sensors and femtosecond laser micromachining.

Changrui Liao was born in Shandong, China, in 1984. He is currently with Shenzhen University, Shenzhen, China, as an Associate Professor. His current research interests focus on femtosecond laser micromachining, optical fiber sensors, and opto-microfluidics.

Xizhen Xu was born in Guangdong, China, in 1990. He received the B.Sc. degree from the College of Science, Zhejiang University of Technology, Hangzhou, China, in 2013, and the M. S. degree in optical engineering from Shenzhen University, Shenzhen, China, in 2016. He is currently working toward the Ph.D. degree in optical engineering at Shenzhen University. His current research interests include optical fiber sensors and fiber Bragg gratings.

Jun He was born in Hubei, China, in 1985. He received the B.Eng. degree in electronic science and technology from Wuhan University, Wuhan, China, in 2006, and the Ph.D. degree in electrical engineering from the Institute of Semiconductors, Chinese Academy of Sciences, Beijing, China, in 2011. From 2011 to 2013, he was with Huawei Technologies, Shenzhen, China, as a Research Engineer. From 2013 to 2015, he was with Shenzhen University, Shenzhen, China, as a Postdoctoral Research Fellow. From 2015 to 2016, he was with The University of New South Wales, Sydney, Australia, as a Visiting Fellow. Since 2017, he has been with Shenzhen University as an Assistant Professor. He has authored or coauthored 4 patent applications and more than 80 journal and conference papers. His current research interests focus on optical fiber sensors, fiber Bragg gratings, and fiber lasers.

Dr. He is a member of the Optical Society of America.

Zhengbiao Ouyang was born in Hunan, China, in 1963. Since 1988, he has been with the College of Electronic Science and Technology, Shenzhen University, Shenzhen, China, where he is currently a Professor. His research interests include photonic crystal and micro photonic sensor.

Yiping Wang (SM'11) was born in Chongqing, China, in 1971. He received the B.Eng. degree in precision instrument engineering from Xi'an Institute of Technology, Xi'an, China, in 1995, and the M.S. and Ph.D. degrees in optical engineering from Chongqing University, Chongqing, China, in 2000 and 2003, respectively. From 2003 to 2005, he was with Shanghai Jiao Tong University, Shanghai, China, as a Postdoctoral Fellow. From 2005 to 2007, he was with the Hong Kong Polytechnic University as a Postdoctoral Fellow. From 2007 to 2009, he was with the Institute of Photonic Technology, Jena, Germany, as a Humboldt Research Fellow. From 2009 to 2011, he was with the Optoelectronics Research Centre, University of Southampton, Southampton, U.K., as a Marie Curie Fellow. Since 2012, he has been with Shenzhen University, Shenzhen, China, as a Distinguished Professor. He has authored or coauthored 1 book, 21 patent applications, and more than 280 journal and conference papers. His current research interests focus on optical fiber sensors, fiber gratings, and photonic crystal fibers.

Prof. Wang is a Senior Member of the Optical Society of America and the Chinese Optical Society.

Maoxiang Hou was born in Hunan, China, in 1990. He is currently a Postdoctoral Research Fellow with Shenzhen University, Shenzhen, China. His main research interests include optical fiber sensing, photonic crystal-fiber and devices, and femtosecond laser micromachining.